Comparison of Measured and Block Structured Simulations for the F-16XL Aircraft

O.J. Boelens[1]

National Aerospace Laboratory NLR, P.O. Box 90502, 1006 BM, Amsterdam, The Netherlands

K.J.Badcock[2]

CFD Laboratory, Department of Engineering, University of Liverpool, L697BZ, UK

A. Elmilgui[3]

Analytical Services and Materials Inc, Hampton, VA, 23666

K.S.Abdol-Hamid[4]

NASA Langley Research Center, Hampton, VA, 23681

and

S.J.Massey[5],

Eagle Aeronautics, Hampton, VA, 23666.

This article presents a comparison of the predictions of three RANS codes for flight conditions of the F-16XL aircraft which feature vortical flow. The three codes, ENSOLV, PMB and PAB3D, solve on structured multi-block grids. Flight data for comparison was available in the form of surface pressures, skin friction, boundary layer data and photographs of tufts. The three codes provided predictions which were consistent with expectations based on the turbulence modelling used, which was k-ε, k-ω with vortex corrections and an Algebraic Stress Model. The agreement with flight data was good, with the exception of the outer wing primary vortex strength. The confidence in the application of the CFD codes to complex fighter configurations increased significantly through this study.

Nomenclature

AVT	=	Applied Vehicle Technology (one of the seven panels within RTO)
BL	=	Butt line on airplane, in.
CAD	=	Computer Aided Design
CAWAP	=	Cranked Arrow Wing Aerodynamics Project
CAWAPI	=	Cranked Arrow Wing Aerodynamics Project International
CFD	=	Computational Fluid Dynamics
C_f	=	Skin friction coefficient $(= \lvert \tau_{nt} \rvert /(\tfrac{1}{2}\rho_\infty u_\infty^2))$
C_p	=	Pressure coefficient $(= (p - p_\infty)/(\tfrac{1}{2}\rho_\infty u_\infty^2))$
FS	=	Fuselage station on airplane, in.
h	=	Airplane altitude, ft.
k	=	Turbulent kinetic energy, ft^2/s^2

---

[1] R&D Engineer, Applied Computational Fluid Dynamics, Department of Flight Physics and Loads, Aerospace Vehicles Division, boelens@nlr.nl.

[2] Professor, Department of Engineering, K.J.Badcock@liverpool.ac.uk

[3] Senior Research Scientist, AIAA Member

[4] Aerospace Engineer, Configuration Aerodynamics Branch, AIAA Associate Fellow

[5] Senior Research Scientist, AIAA Member

LES	=	Large Eddy Simulation
L_{ref}	=	Reference length, in.
M	=	Mach number
$NASA$	=	NATIONAL Aeronautics and Space Administration
$NATO$	=	North Atlantic Treaty Organization
NLR	=	Nationaal Lucht- en Ruimtevaartlaboratorium, Netherlands National Aerospace Laboratory
$PAB3D$	=	Propulsion Aerodynamics Branch 3D URANS solver
$PANS$	=	Partially Averaged Navier-Stokes
PMB	=	Parallel Multiblock
p	=	Pressure, psia
p_s	=	Static pressure, psia
p_t	=	Total pressure ($= p(1 + \frac{1}{2}(\gamma-1)M^2)^{\frac{\gamma}{\gamma-1}}$, psia
p_∞	=	Free-stream pressure, psia
P_k	=	Production of turbulent kinetic energy
$P_k^{\ u}$	=	Unlimited production of turbulent kinetic energy
r	=	Ratio of the magnitude of the rate-of-strain and vorticity tensors
$RANS$	=	Reynolds-averaged Navier-Stokes
Re, R_n	=	Reynolds number
RTO	=	Research and Technology Organization – scientific arm of NATO
S	=	Simulation
S_{ij}	=	Mean flow strain rate, s^{-1}
SZL	=	Shih-Zhu-Lumley
T	=	Temperature, °R
T_s	=	Static temperature, °R
T_t	=	Total temperature ($= T(1 + \frac{1}{2}(\gamma-1)M^2)$, °R
TNT	=	Turbulent non-turbulent
TVD	=	Total variation diminishing
u	=	Velocity, ft/s
$\boldsymbol{u}$	=	Velocity vector, ft/s
u_∞	=	Free-stream velocity, ft/s
$URANS$	=	Unsteady Reynolds-averaged Navier-Stokes
VFE	=	Vortex Flow Experiment
V/V_{RE}	=	Ratio of velocity magnitude in boundary layer to that at the Rake Extreme total-pressure tube
x/c	=	Fractional distance along the local chord, positive aft
y/s	=	Fractional distance along the local span, positive outward
y^+	=	Re-like term for flat plate turbulent boundary layer
z	=	Normal distance above the surface at a rake location, mm
α	=	Angle of attack, °
β	=	Side-slip angle, °
γ	=	Specific heat ratio (=1.4)
ρ	=	Density, slugs/ft^3
ρ_∞	=	Free-stream density, slugs/ft^3
Ω_{ij}	=	Vorticity, s^{-1}
τ_{nt}	=	Tangential component of the total stress tensor, psia
ω	=	Specific turbulent dissipation rate, 1/s

I.   Introduction

Application of Computational Fluid Dynamics (CFD) methods to support the operation of fighter aircraft requires realism and cost-effectiveness compared with alternatives such as wind-tunnel tests or flight tests. Two envisaged applications of CFD are for the assessment of stability and control characteristics, and the calculation of changes in aircraft loads due to new store configurations. By using CFD the number of flight

conditions in a flight test certification program can be optimized and potentially dangerous cases can be identified beforehand. To enable application of CFD methods for such purposes, the methods should be well validated and evaluated against state-of-the-art wind tunnel and/or flight test data.

The Cranked-Arrow Wing Aerodynamics Project (CAWAP) [1] provided the CFD community with an excellent database for validation and evaluation purposes. This project focused on the understanding of flow phenomena encountered on the cranked-arrow wing of the F-16XL aircraft. The CAWAP database contains both subsonic and transonic data at flight Reynolds numbers. The data obtained during the flight tests comprised surface pressure measurements, both along butt line stations and fuselage stations, boundary layer measurements at four positions on the left wing, skin friction measurements at the FS330 station on the left wing and surface flow visualizations using tufts.

Initiated by NASA, the Cranked-Arrow Wing Aerodynamics Project International (CAWAPI) [2]-[6] was started as a follow-on project. Along with the Vortex Flow Experiment 2 (VFE-2) [7], this project was incorporated under the NATO RTO working group AVT-113. This article reports on contributions to CAWAPI made by National Aerospace Laboratory NLR, University of Liverpool and NASA Langley made using structured multi-block flow solvers.

This article continues with a summary of the flow solvers used. The generation of a common grid is summarised and then results are compared for several flight conditions that feature vortical flow. Finally the performance of the solvers is evaluated and conclusions are drawn.

II.   Flow solvers

A. NLR Solver (ENSOLV)

The flow solver ENSOLV, which is part of NLR's flow simulation system ENFLOW [8], is capable of solving the Euler and Navier-Stokes equations on multi-block structured grids for arbitrary configurations. The configuration can be either fixed or moving relative to an inertial reference frame, and can be either rigid or flexible. The equations in full conservation form are discretized in space by a second-order accurate, cell-centred, finite-volume method, central differences, and matrix artificial diffusion. The artificial diffusion consists of a blending of second-order and fourth-order differences with a Jameson-type shock sensor for the basic flow equations and a TVD discontinuity sensor for the turbulence model equations. For steady flow simulations, the discretized time-dependent

system of equations is integrated toward the steady-state solution using a five-stage explicit Runge-Kutta scheme. Local-time stepping, implicit residual averaging and multi-grid acceleration techniques are applied.

B. Liverpool Solver (PMB)

The PMB solver [9] has been under development at the Universities of Glasgow and Liverpool during the past decade. The Euler and RANS equations are discretised on curvilinear multi-block body conforming grids using a cell-centred finite volume method which converts the partial differential equations into a set of ordinary differential equations. The convective terms are discretised using Osher's upwind method. Monotone Upwind Scheme for Conservation Laws variable extrapolation is used to provide second-order accuracy with the Van Albada limiter to prevent spurious oscillations around shock waves. Following Jameson, the spatial residual is modified by adding a second order discretisation of the real time derivative to obtain a modified steady state problem for the flow solution at the next real time step, which is solved through pseudo time. This pseudo time problem is solved using an unfactored implicit method, based on an approximate linearisation of the residual. The linear system is solved in unfactored form using a Krylov subspace method with Block Incomplete Upper Lower preconditioning. The preconditioner is decoupled between blocks to allow a high efficiency on parallel computers with little detriment to the convergence of the linear solver. For the Jacobian matrix of the CFD residual function, approximations are made which reduce the size and improve the conditioning of the linear system without compromising the stability of the time marching.

C. PAB3D Solver

The PAB3D CFD code [10] is a structured, multi-block, parallel, implicit, finite-volume solver of the three-dimensional RANS equations. Advanced turbulence models are available in the code. Viscous models include coupled and uncoupled Navier-Stokes and thin layer Navier-Stokes options. Roe's upwind scheme is used to evaluate the explicit part of the governing equations, and van Leer's scheme is used for the implicit part. Diffusion terms are centrally differenced. PAB3D utilizes either a 2-factor or 3-factor numerical scheme to solve the governing equations. For unsteady calculations, PAB3D is second order in time with sub iterations. For steady state calculations, local time stepping and grid sequencing are applied to accelerate convergence. PAB3D is widely used for internal and external flow applications by NASA and by the US aerospace industry. PAB3D has several built-in time saving routines, including grid sequencing and distributed computer memory requirements, that permit the user

American Institute of Aeronautics and Astronautics

to quickly obtain a converged solution. There are several state-of-the-art two-equation and algebraic Reynolds stress turbulence models implemented. In an attempt to increase the fidelity and accuracy, multi-scale-type (hybrid) turbulence models: URANS/LES [11] and Partially Averaged Navier-Stokes PANS [12] have been added to the code. PAB3D has been well-tested and documented for the simulation of aero-propulsive and aerodynamic flows involving separation, mixing, and other complicated phenomena. PAB3D is ported to a number of platforms and offers a combination of good performance and low memory requirements. In addition to its advanced pre-processor, which can handle complex geometries through multi-block general patching, PAB3D has a runtime module capable of calculating aerodynamic performance on the fly as well as a post processor used for follow-on data analysis.

For this study, PAB3D used third order Monotone Upwind Scheme for Conservation Laws variable extrapolation of the fluxes with MINMOD limiter, and the upwind flux difference splitting of Roe for evaluating the convective terms. Viscous diffusion terms were modeled as uncoupled in the flow direction and fully coupled in the cross-flow direction. A 3-factor scheme was used for the approximation of implicit terms. Local time stepping and grid sequencing were applied to accelerate convergence.

D. Turbulence Models

1. Basic models

The test cases which were computed for this article feature the flow over the F-16XL aircraft, with extremely complex geometry, at flight Reynolds numbers. The flows themselves are complex with multiple vortices present. The complex geometry provides a grid generation challenge, which is considered in the next section. The complex flow field provides a challenge to the turbulence modeling. In the current section the options used for this modeling are summarized. All calculations were made assuming fully turbulent flow.

The basic Boussinesq models were of the 2 equation type. For ENSOLV, the TNT k-ω model, which is a variant of the Wilcox k-ω model, is employed. The equations of the model are slightly modified by the introduction of a 'cross diffusion' term [13]. This modification has been introduced to resolve the dependency of the free-stream-valued of ω. In addition, to remove the singular behaviour of ω at solid boundaries, the equations of the k-ω model are reformulated such that instead of ω the quantity $\tau=1/(\omega+\omega_0)$ is used. Here ω_0 is a positive constant (default value $\omega_0 L_{ref}/u_\infty=20$, with U_∞ the free-stream velocity and L_{ref} the reference length). At the solid boundaries, both k and τ are set to zero. To prevent unphysical high values of k near stagnation points, the production term in the k-equation has been limited to a maximum of 20 times the dissipation term in the k-equation. At the 'inflow' parts of the far-

field boundary, the free-stream values of the turbulent variables are computed from the free-stream turbulent Reynolds number (0.01 in the present simulations) and the free-stream dimensionless turbulent kinetic energy ($k/u_\omega^2 = 10^{-6}$ in the present simulations). For PMB the standard k-ω model was used. Finally, for PAB3D the standard k-ε model was used. In addition, the PAB3D code also presented results using the Shih-Zhu-Lumley (SZL) algebraic stress model [14], where the stress equation is given by:

$$-\overline{u_j u_i} = -\frac{2}{3}\delta_{ji}k + 2C_\mu \frac{k^2}{\varepsilon}\ S_{ji} - 2\beta \frac{K^3}{\varepsilon^2}(\Omega_{ik}\overline{S}_{kj} - \overline{S}_{ik}\Omega_{kj})$$

where

$$C_\mu = \left(A_o + A_s^* \frac{U^* k}{\varepsilon}\right)^{-1};\ \Omega_{ij} = \frac{1}{2}(\frac{\partial u_i}{\partial x_j} - \frac{\partial u_j}{\partial x_i});\ \ \overline{S}_{ij} = S_{ij} - \frac{1}{3}S_{kk}\delta_{ij};\ S_{ij} = \frac{1}{2}(\frac{\partial u_i}{\partial x_j} + \frac{\partial u_j}{\partial x_i})$$

Note the higher order nonlinear terms involving the deviatoric mean flow strain rate ($\overline{S}_{ij}$) and vorticity (Ω_{ij}) tensors in the stress equation. In the C_μ equation, $A_0 = 6.5$, and **C_2**, A_s^*, and U^* involve tensor products of S_{ij} and Ω_{ij} and their variants. Algebraic stress models give inherently better results than the linear stress model because of the explicit modeling of effects such as relaxation and the specific inclusion of nonlinear anisotropic effects from the mean flow strain and vortices.

2. Enhanced vortex correction model

Boussinesq models over predict the eddy viscosity within the vortex core, leading to exaggerated diffusion of vorticity. As a consequence the details of the vortex core are lost and low suction peaks with wide vortex bases are a characteristic of the solution. For this reason an enhanced vortex correction model [15] [16] is used that controls the production of turbulent kinetic energy and hence eddy viscosity through either an increase in the production of dissipation (ω) or a decrease in the production of turbulent kinetic energy within regions of highly rotational flow. To illustrate, in the second variant, the production of turbulent kinetic energy k is limited as

$$P_k = \min\{P_k^u, (2.0 + 2.0 \times \min\{0, r-1\})\rho\beta^* k\omega\}$$

Here P_k^u is the unlimited production of k and r is the ratio of the magnitude of the rate-of-strain and vorticity tensors. This approach has proven to be effective in producing surface pressure profiles on simple delta wings in good agreement with those of experimental data [15] [16]. The results presented in this article for the ENSOLV

solver uses the ω-enhanced version of this method based on the TNT k-ω model described above. The PMB results used the k-limited variant based on the k-ω model.

3. Summary

In summary, the ENSOLV results have been obtained using the TNT k-ω model with a ω enhancer vortex correction. The PMB calculations used the standard k-ω model with a k-limited vortex correction. PAB3D used the k-ε model and the SZL Algebraic Reynolds Stress model.

III.   Grid generation

A common grid for the block structured solvers was generated by NLR. The approach to grid generation is described in reference [3] and is not repeated here. Two small modifications to the surface description were made to further facilitate the generation of a structured grid. First, a small 'step' or 'plate' on the wing upper surface was removed. Secondly, the end part of the vertical tail base was slightly rounded off. Apart from these changes, the original definition of the geometry as given in the CAD model was respected. The final grid was produced in less than 4 weeks, including some development of the grid generation tools. This time compared favourably with that required to produce the unstructured grids in CAWAPI.

The following family of structured grids has been used:

- The baseline structured grid around the half-span full-scale model of the F-16XL consisting of 1903 blocks, 14,750,720 grid cells and 17,014,119 grid points.

- The baseline structured grid with a reduced number of blocks. The merging step resulted in a reduction of the number of blocks from 1903 to 216.

- A structured grid around the full-scale model of the F-16XL consisting of 3806 blocks, 29,501,440 grid cells and 34,028,238 grid points. This grid has been generated by mirroring the baseline structured grid around the half-span full-scale model of the F-16XL with respect to the symmetry plane.

The upper surface grid and the resulting y^+ distribution over the upper surface are shown in reference [3], Fig. 7. From this figure, it is evident that the grid spacing normal to the surface has a desired value of y^+ less then one (based on an ENSOLV solution), except for the regions below the vortical structures.

IV. Results for Vortical Flow Flight Conditions

A. Flight test cases

Initially four flight conditions were selected for computation in CAWAPI of which three featured vortical flow. Later three additional flight conditions were added to the original set. These additional flight conditions also featured vortical flow, with flight condition 25 at higher incidence and the other two conditions (flight condition 50 and 51) exhibiting side-slip. Only the vortical flow conditions are of interest in the current article and these are summarised in Table 1. Conditions 7, 19, 25 and 46 have zero side slip and were computed by all three codes using the baseline structured grid around the half-span full-scale model of the F-16XL. Conditions 50 and 51, which have non-zero sideslip, were computed using ENSOLV and PAB only using the structured grid around the full-scale model of the F-16XL. Results for all flight conditions can be found in reference [6]. In the current article results for flight conditions 7, 19 and 46 were evaluated in detail.

Table 1: CAWAPI flight conditions

Flight condition		Nominal						Actual			
		α, °	β, °	h, ft	M	10^6 R_n/ft		α, °	β, °	M	Re
7		13	0	5000	0.29	1.79		11.89	-0.133	0.304	44.40 10^6
19		13	0	10000	0.32	1.71		11.85	0.612	0.360	46.80 10^6
25		20	0	10000	0.24	1.28		19.84	0.725	0.242	32.22 10^6
46		10	0	24000	0.51	1.77		10.40	0.310	0.527	46.90 10^6
50		13	5	24000	0.42	1.46		13.56	5.310	0.434	38.41 10^6
51		13	-5	24000	0.42	1.46		12.89	-4.580	0.441	38.95 10^6

Engine flow conditions were specified in CAWAPI and engine face and jet boundary conditions, based on this data, were used in the ENSOLV and PAB solutions. In ENSOLV, at the inlet duct exit plane (engine inlet) a prescribed normalized static pressure p/p_∞ was used, whereas at the mixing plane (engine exit) a boundary condition with a prescribed normalized total pressure $p_t/p_{t,\infty}$ and total temperature $T_t/T_{t,\infty}$ was applied. For PAB3D, constant total values were specified for the nozzle inlet, and constant pressure boundary condition was specified at the nozzle exit. Preliminary calculations using ENSOLV, and all of the PMB calculations, used a simple flow through condition, where the engine face and jet plane were treated as far field boundaries. This treatment did not noticeably influence the predictions of the vortical flow on the upper surface of the wing and therefore no further discussion of the engine boundary conditions is made in this article.

B. Overview of Flow Topology

Before looking to the results in detail, the large-scale vortical flow structure above the wing is discussed. Fig. 1 shows an iso-surface of the vorticity magnitude for flight condition 7. The flow structure consists of several vortices: i) the inner wing primary vortex originating from the wing leading edge inboard of the crank, ii) outer wing vortex originating from the wing leading edge outboard of the crank, iii) the air dam vortex originating form the air dam at wing upper surface, iv) the missile vortices originating from the missile fins and v) the fuselage vortex. In addition to these vortices other vortical structures, such as for example the inner wing secondary vortex, are present. All flight conditions characterized by vortical flow exhibit a similar vortical flow structure, although the strength and location of the vortices may differ.

C. Comparison with Flight Data

The predictions are now compared against available flight data. Note that the common flight conditions chosen in CAWAPI did not match exactly the conditions of the flight data, and in particular the angle of incidence is lower in the computations than the measurements for the comparisons shown here. This is likely to have the effect of making the primary vortices weaker in the computational results, with lower suction in the footprint on the wing. Computational results were available from the vortex correction variants of the k-ω models in ENSOLV and PMB, and from the k-ε and ASM models in PAB3D.

The comparison for the surface pressure coefficient is shown in Fig. 2 for three butt lines (BL's), 80, 95 and 153.5, going progressively outboard. The general agreement for the two BL's inboard of the crank is good. The ENSOLV predictions show similar suction levels for the primary vortex. The PMB and PAB3D k-ε predictions have weaker vortices, with the PMB solution showing a more compact vortex footprint. The comparisons at BL 80, showing the lack of a flat region in the C_p-distribution close to the leading edge, indicate that the strength of the secondary inboard vortex is under predicted. The secondary vortex appears to have developed more fully by BL90. The comparisons outboard of the crank, at BL153.5, are less favourable. The suction in the primary outboard vortex is significantly less than the measurements in all predictions.

The boundary layer profiles are compared in Fig. 3. Three inboard rake locations are used, with one being inboard of the primary vortex, the second underneath the primary vortex, and the third in the region of the secondary vortex. The general agreement with flight measurements is again good, and ENSOLV and PMB are also close. For

the rake closest to the leading edge the ASM model and the vortex correction models give a fuller profile than the measurements and the k-ε predictions.

The comparison of the skin friction values along a fuselage station is shown in Fig. 4. The PMB prediction, which has not been extracted, is not included. The comparisons show that the levels under the primary vortex agree well with the measurements, with the PAB3D predictions being lower than those from ENSOLV. Again there is more discrepancy under the secondary vortex, with levels being too high from ENSOLV, and more in line with the measurements for PAB3D. The k-ε predictions show the wrong shape in this region but the ASM predictions are closest to the measurements.

Finally, the comparison between surface streamlines from the ENSOLV solution, and tufts from the flight tests, is shown in Fig. 5. The black dots visible are calibration targets. Inboard of the crank the agreement in the flow direction as indicated by the tufts and surface streamlines is good. The re-attachment line of the inner wing primary vortex and the separation line of the inner wing secondary vortex are clearly visible. The agreement in the flow direction outboard of the crank is less good. It is noted that here the tufts have a blurred character, indicating local unsteadiness of the flow.

D. Evaluation

The comparisons with flight data indicate that the CFD predictions are generally good. However, some flow details are not well represented and these are considered in the current section. It is observed that the wing leading edge geometry, and the high Reynolds number, are both helpful to the CFD in the sense that the prediction of the initial flow separation around the leading edge is made easier. First, the geometry towards the fuselage S-blend contains a flat strip at the section leading edge which has the effect of producing a sharp corner. This corner fixes the separation point and so the problem of predicting a smooth body separation, which is a challenge for CFD, is not present, at least when the inner wing primary vortex is becoming established. The leading edge at the crank is very sharp, meaning the same situation holds at the formation of the primary outboard vortex. Further, the high Reynolds number means that the leading edge flow is likely to be fully turbulent, avoiding any influence of transition. Flow separation in all solutions was observed to be right at the section leading edge, both inboard and outboard of the crank, as indicated in Fig. 6.

The upper wing flow is very complex with a number of separations and reattachments, as illustrated in Fig. 6. The surface streamline pattern in this figure is composed of the following main elements:

a) *The primary separation on the inner and outer wing.* The flow separates on the wing leading edge. On the part of the wing in board of the crank this separation results in the inner wing primary vortex, whereas on the part of the wing out board of the crank the outer wing vortex is formed.

b) *The primary re-attachment on the inner wing.* At this line the vortical flow associated with the inner wing primary vortex re-attaches on the wing surface. Note that for the present case the inner wing primary vortex lifts off of the surface, resulting in a fanning out of the re-attachment line.

c) *The secondary separation on the inner wing.* Underneath the inner wing primary vortex the flow separates resulting in the inner wing secondary vortex. This separation line starts some distance downstream of the apex of the wing and is present up to the wing trailing edge.

d) *The secondary re-attachment on the inner wing.* At this line the vortical flow associated with inner wing secondary vortex re-attaches to the wing surface. This re-attachment line extends until the leading edge of the air dam.

e) *The re-attachment on the inner wing side of the air dam.* After reaching the air dam the vortical flow resulting from the inner wing secondary vortex re-attaches to the inner wing side of this air dam. Note that this re-attachment line is a continuation of the secondary re-attachment line on the inner wing. When the air dam changes to the actuator pod this re-attachment line stops to exist, and the vortical flow associated with the inner wing secondary vortex re-attaches in the junction between the actuator pod and the wing.

f) *The separation from the edge of the air dam.* The flow separates from the upper edge of the air dam. This separation results in the air dam vortex.

g) *The separation on the actuator pod.* The flow separates from the upper side of the actuator pod. Note that this separation starts before the intersection of the air dam and the actuator pod. The air dam vortex is fed further by the flow coming from this separation.

h) *The re-attachment on the outer wing of the outer wing vortex and the air dam vortex.* At this line the vortical flows associated with both the outer wing vortex and the air dam vortex re-attach.

i)   *The separation due to the air dam vortex.* Due to the air dam vortex the flow separates just outboard of the air dam. This separation results in a small vortex in the outboard junction region between the air dam and the wing surface.

j)   *The re-attachment on the outer wing side of the air dam.* The vortical flow associated with the small vortex described in i) re-attaches to the air dam at this line.

The different turbulence options provided results which followed a pattern. The k-ε model predicted weaker vortices due to the excessive levels of turbulence produced. The ASM produced a stronger inner wing primary vortex, as shown in Fig. 7 for FC46. The vortex correction models also fixed this problem, and realistic levels of suction under the primary inboard vortex were obtained with a simple correction to the underlying k-ω models.

Inboard of the crank, problems were noted with the strength of the inner wing secondary vortex. The grid in the region concerned was observed to be somewhat coarse, meaning that no conclusions could be drawn about the performance of the physical modelling there.

The most important discrepancy arising from the comparisons is the very weak primary vortex predicted outboard of the crank. The flow in this region is very complex, featuring the primary and secondary inner wing vortices, the outboard primary and secondary vortices, and also vortices that have arisen from the interaction of the inboard vortices with the air dam. There are two main possibilities for the weakness of the predicted outboard primary vortex. First, the levels of turbulence predicted for the PMB solution are shown in Fig. 8. The turbulent Reynolds number plotted is defined as the ratio of the eddy viscosity to the molecular viscosity, and is an indication of how much more viscous the flow is from the contribution of the turbulence model. Low levels of turbulence are indicated in blue and high levels in red. The influence of the vortex correction on the inner wing vortex and the vortex arising from the interaction with the air dam can be seen. However, the outer wing primary vortex is filled with red, indicating high levels of turbulence there, explaining its weakness. The flow in this region is complex, with regions of shear between different vortices. The simple vortex correction appears to fail because the levels of turbulence in the outer wing vortex are not simply down to production terms, but to convection of turbulence also. Interesting, the more general ASM also fails to predict the outboard primary vortex strength close to the measurements and this may be due to the coarse nature of the computational grid in the area of interest. To better

resolve the outer primary vortex one needs a finer grid along the full trajectory of the vortex core or to use grid adaption methodology that will cluster points in areas of high flow gradients.

The second consideration in this region is the likely presence of unsteady flow when several vortices are in close proximity. Evidence for this comes from the photographs of the tufts from the flight tests, which are blurred in this region. All of the computations presented in this article assumed steady state flow.

E. Assessment of Solver Performance

The ENSOLV calculations used grid sequencing on three levels and a two-level full approximation storage multi-grid scheme to solve on the two finer grid levels. The simulations were performed on two processors of NLR's NEC SX5/8B vector computer. Four orders of convergence were obtained for the root mean square norms. Larger block dimensions result in an increase of the vector length, and merging the blocks (see section III) resulted in a reduction of the required computational time by a significant factor of around 4. The final calculation of a flight condition required around 16 hours, and 1200 fine grid multigrid cycles.

The PAB3D solution also used two levels of grid sequencing. The calculations were run on a cluster with 2.8GHz processors. A typical calculation on 56 processors gave a converged solution in 51 wall clock hours and ten thousand fine grid iterations.

The PMB calculations were made on the Liverpool University CFD Laboratory cluster which has 192 processors with a clock speed of 3.4GHz. The calculations required around 2 days on 96 processors, with up to twenty thousand iterations required to reach convergence. No grid sequencing was used. The main difficulty with the calculations was the small CFL number required to avoid divergence. For difficult cases involving large gradients it is usual to for PMB to run with a CFL number of 5. However, the current calculations required a CFL number of 1 or 2, leading to a large number of iterations to convergence. One possible reason for the relatively poor performance is the flow behind the tip missile, which appeared to be unsteady. The probability of unsteady flow outboard of the crank could also be a reason.

VI Conclusion

This article presented and evaluated results obtained from three multi-block RANS solvers for the F-16XL aircraft. The following conclusions are drawn

American Institute of Aeronautics and Astronautics

1. The generation of a good quality grid was achieved by NLR in a time comparable to that required for the generation of unstructured grids within CAWAPI.

2. The agreement between the 3 codes was generally good, with the expected dependence on the turbulence modelling observed.

3. The inner wing primary vortex was well predicted by the vortex correction based turbulence models, offering an easy way to implement a correction to standard 2 equation Boussinesq models.

4. The outboard primary vortex was not predicted well by any code, perhaps due to unsteady flow in this region.

5. Computational wall clock time of one to two days was observed for all three codes.

Acknowledgments

References

[1] Lamar, J.E., Obara, C.J., Fisher, B.D, and Fisher, D.F., "Flight, wind-tunnel, and Computational Fluid Dynamics Comparison for Cranked Arrow Wing (F-16XL-1) at Subsonic and Transonic Speeds," NASA TP-2001-210629, 2001.

[2] Obara, C.J.; and Lamar, J.E., "Overview of the Cranked-Arrow Wing Aerodynamics Project International," *AIAA Journal of Aircraft*, published online xx xxx. 2007. doi: xx.xxx/x.xxxxx

[3] Boelens, O.J., Badcock, K.J., Görtz, S., Morton, S., Fritz, W., Karman Jr., S.L., Michal, T. and J.E. lamar, "Description of the F-16XL geometry and computational grids used in CAWAPI," *AIAA Journal of Aircraft*, published online xx xxx. 2008. doi: xx.xxx/x.xxxxx

[4] Goertz, S., Jirasek, A., Morton, S.A., McDaniels, D.R., Cummings, R.M.; Lamar, J.E., and Abdol-Hamid, K.S., "Standard Unstructured Grid Solutions for CAWAPI F-16XL," *AIAA Journal of Aircraft*, published online xx xxx. 2008. doi: xx.xxx/x.xxxxx

[5] Fritz, W., Davis, M.B., Karman, S.L., Jr., and Michal, T., "RANS Solutions for the CAWAPI F-16XL Using Different Hybrid Grids," *AIAA Journal of Aircraft*, published online xx xxx. 2008. doi: xx.xxx/x.xxxxx

[6] Rizzi, A., Jirasek, A., Badcock, K.J., Lamar, J.E., Boelens, O.J., and Crippa, S., "What Was Learned from Numerical Simulations of F-16XL (CAWAPI) at Flight Conditions," *AIAA Journal of Aircraft*, published online xx xxx. 2008. doi: xx.xxx/x.xxxxx

[7] Hummel, D., and Redeker, G., "A New Vortex Flow Experiment for Computer Code Validation," *RTO-AVT Symposium on Advanced Flow Management; Part A - Vortex Flow and High Angle of Attack Papers on Disc* [CD-ROM], Paper Number 8, May, 2001.

[8] Boerstoel, J.W., Kassies, A., Kok, J.C., and Spekreijse. S.P., "ENFLOW, a Full-Functionality System of CFD Codes for Industrial Euler/Navier-Stokes Flow Computations," NLR TP 96286U, NLR, Amsterdam, 1996.

[9] Badcock, K.J., Richards, B.E. and Woodgate, M.A., "Elements of Computational Fluid Dynamics on Block Structured Grids using Implicit Solvers," *Progress in Aerospace Sciences*, vol 36, 2000, pp 351- 392.

[10] Abdol-Hamid, K., Pao, S.P., Hunter, C., Deere, K.A., Massey, S.J. and Elmiligui, A., "PAB3D: Its history in the use of Turbulence Models in the Simulation of Jet and Nozzle Flows", AIAA-2006-0489, 2007.

[11] Nichols, R.H. and Nelson, C.C., "Application of Hybrid RANS/LES Turbulence Models," AIAA-2003-0083, 2003.

[12] Abdol-Hamid, K. and Girimaji, S., "A Two-Stage Procedure Toward the Efficient Implementation of PANS and Other Hybrid Turbulence Models," NASA TM-213260, 2004.

[13] Kok, J.C., "Resolving the dependence on free-stream values for the k-ω turbulence model", NLR-TP-99295, NLR, Amsterdam, 1999.

[14] Shih, T.H., Zhu, J. and Lumley, J.L., "A New Reynolds Stress Algebraic Equation Model," NASA TM-106644, August 2004.

[15] Brandsma, F.J., Kok, J.C, Dol, H.S. and Elsenaar, A., "Leading edge vortex flow computations and comparison with DNW-HST wind tunnel data," NLR-TP-2001-238, NLR, Amsterdam, 2001.

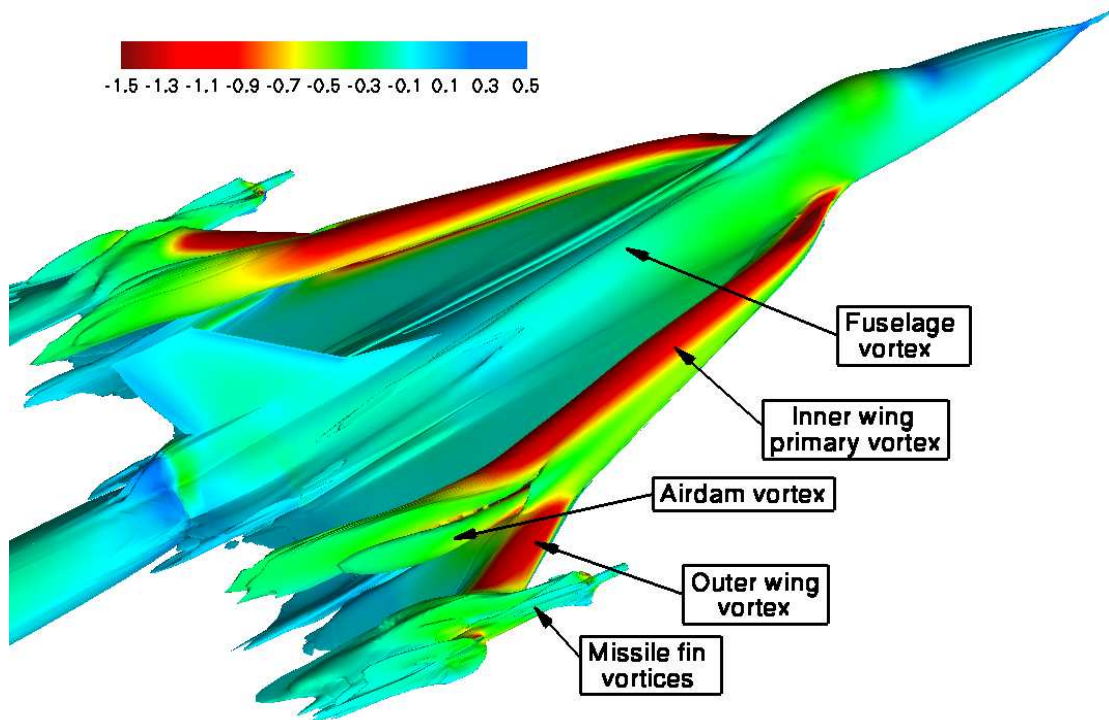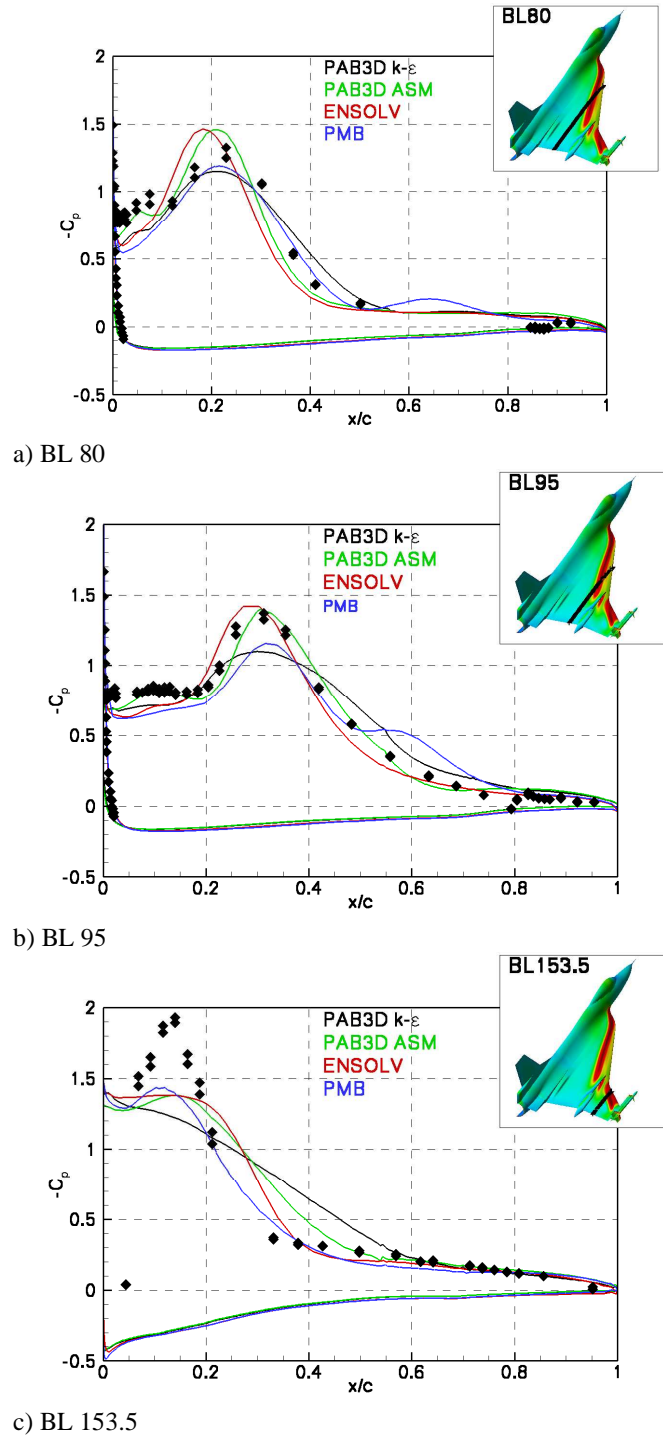[16] Dol, H.S., Kok, J.C. and Oskam, B., "Turbulence modeling for leading-edge vortex flows," AIAA-2002-0843, 2002.

Fig. 1: Iso-surface (level equals 250 Hz) of vorticity magnitude for flight condition 7 (α=11.89°, M=0.304 and Re=44.40 10[6]). The vortices are colored by the pressure coefficient C_p.

American Institute of Aeronautics and Astronautics

a) BL 80

b) BL 95

c) BL 153.5

Fig. 2: Surface pressure coefficient for flight condition 7 (α=11.89°, M=0.304 and Re=44.40 10⁶) and flight condition 19 (α=11.85°, M=0.360 and Re=46.80 10⁶) along butt lines: a) BL55, b) BL80, c) BL 95.

American Institute of Aeronautics and Astronautics

a)

b)

c)
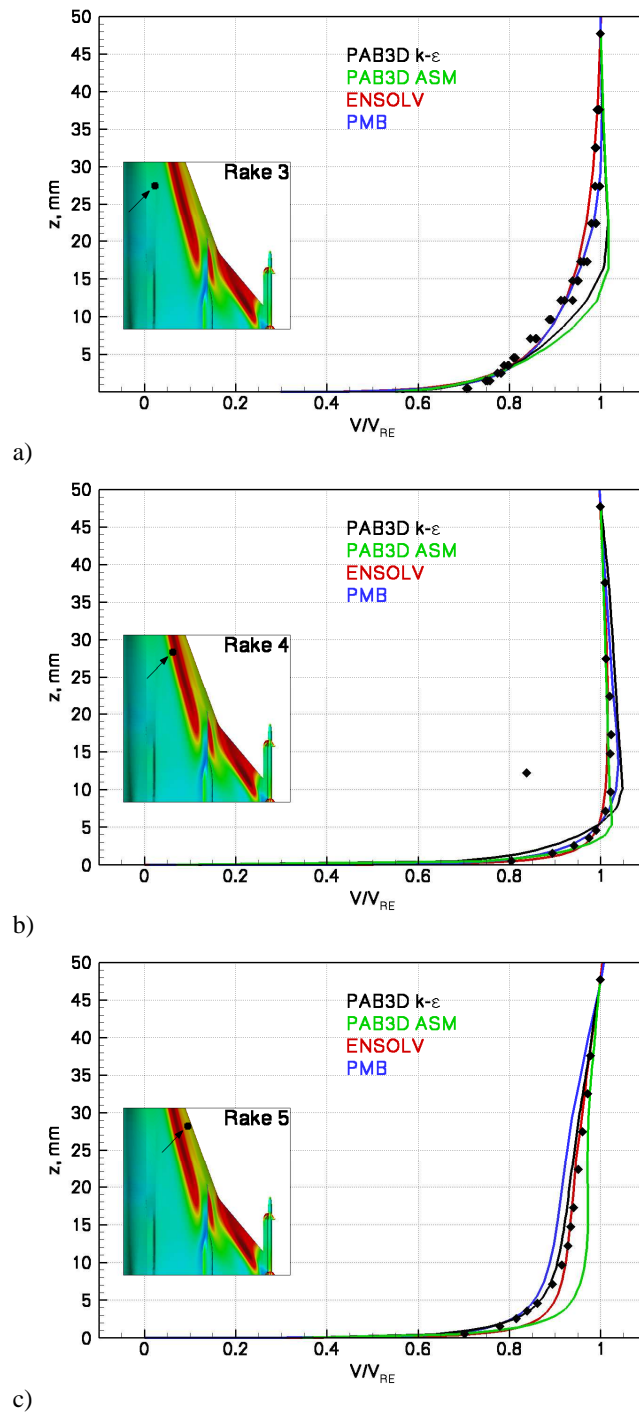
Fig. 3: Boundary layer profiles for flight condition 7 (α=11.89°, M=0.304 and Re=44.40 10^6).

American Institute of Aeronautics and Astronautics
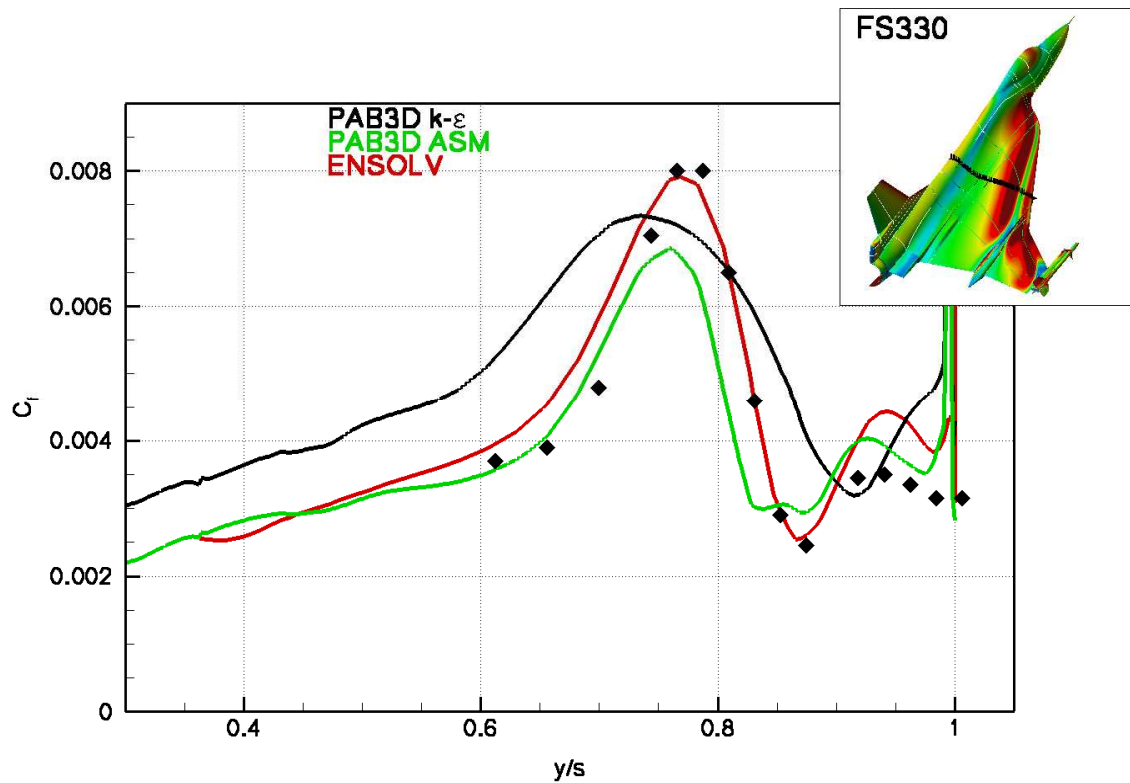
Fig. 4: Local skin friction coefficient for flight condition 19 ($\alpha=11.85°$, M=0.360 and Re=46.80 10^6) at FS300 (dashed line) and FS330 (solid line).
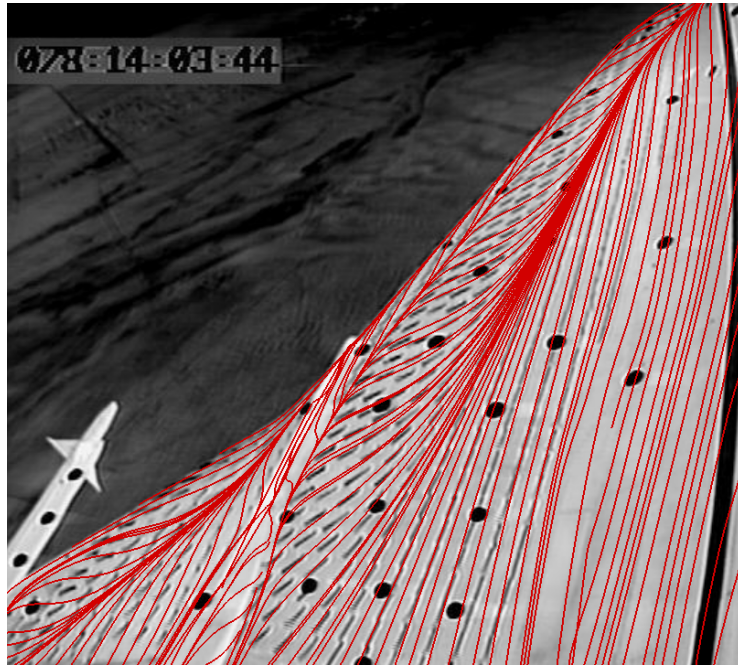
American Institute of Aeronautics and Astronautics

Fig. 5: Surface streamlines superimposed on the negative of the tuft image for flight condition 7 (α=11.89°, M=0.304 and Re=44.40 10[6]), Flight 145, Run 16b, Video (yr, 1996), 078:14:03:44 (Day:hr:min:sec).
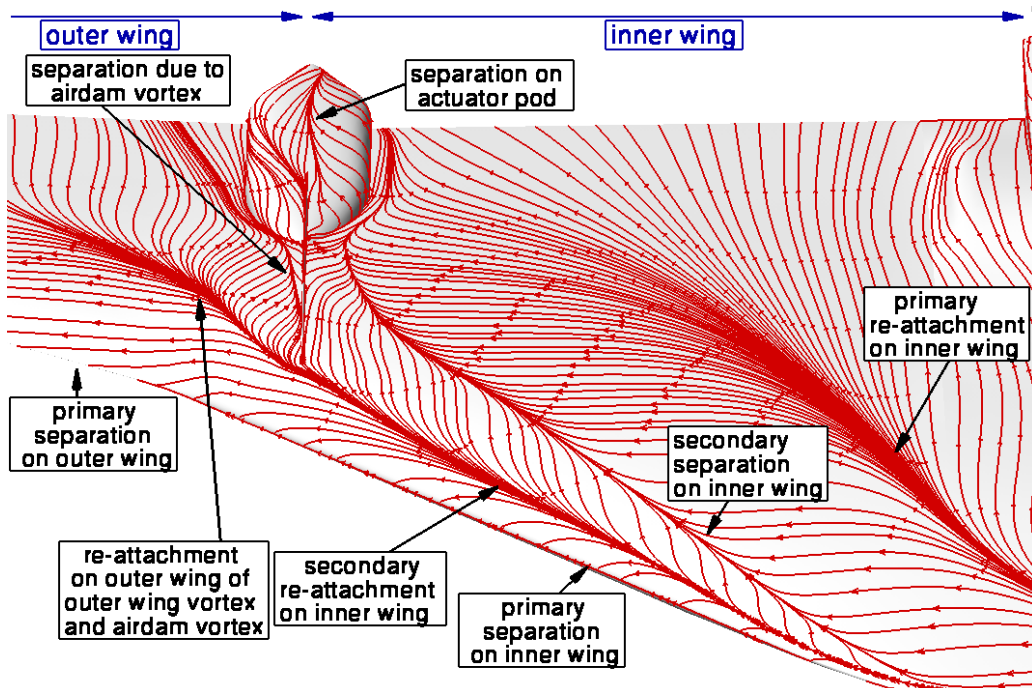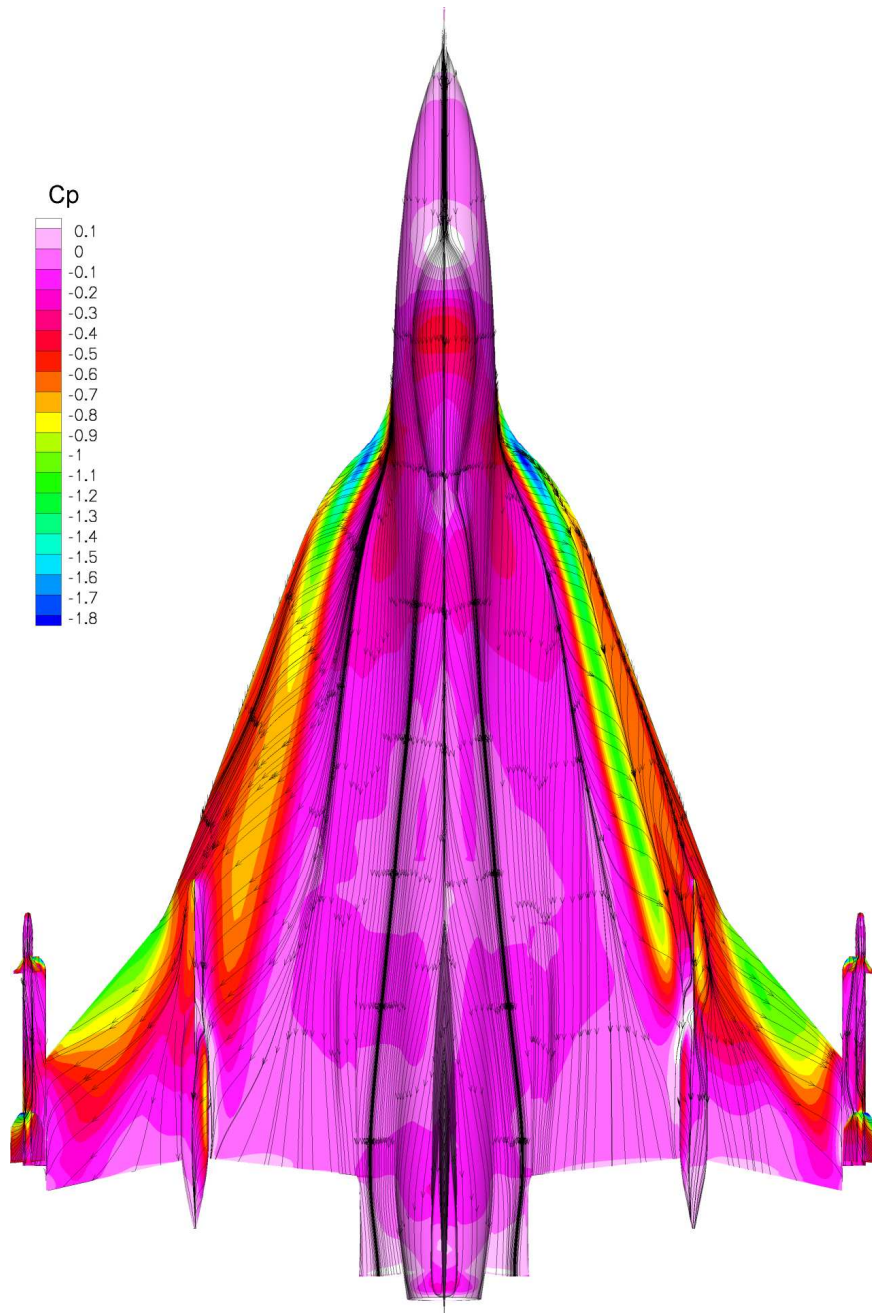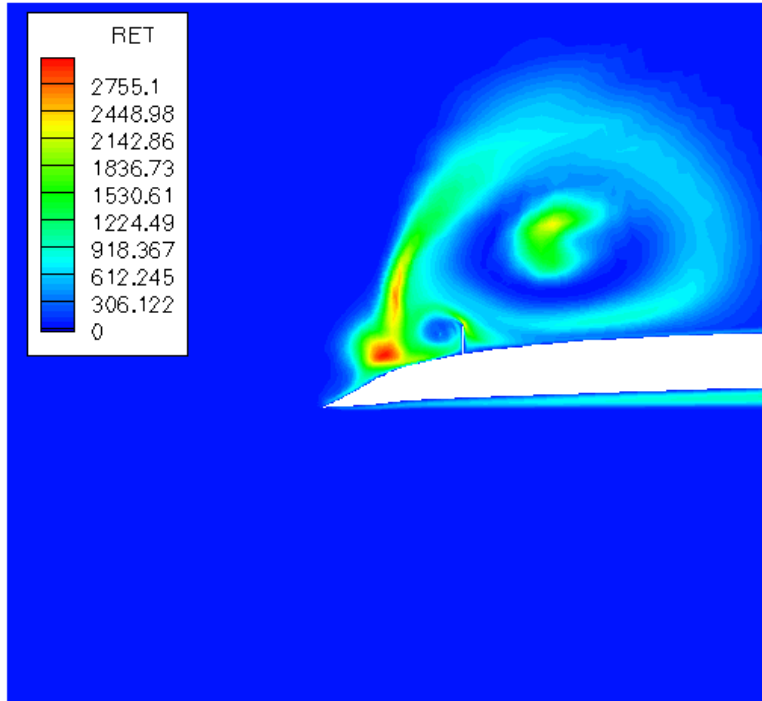

Fig. 6: Surface streamline pattern for flight condition 7 (α=11.89°, M=0.304 and Re=44.40 10[6]), overview of the surface streamline pattern.

American Institute of Aeronautics and Astronautics

Fig. 7:. Upper surface pressure distribution with streamlines flight condition 46 (α = 10.4°, M=0.527 and Re=46.9 10^6).

Fig. 8: Contours of turbulent Reynolds number for flight condition 7(α=11.89°, M=0.304 and Re=44.40 10^6) on a spanwise slice just downstream of the crank. Here the turbulent Reynolds number is the ratio of the eddy viscosity to the molecular viscosity.

American Institute of Aeronautics and Astronautics